

Optimal Disturbances in the Supersonic Boundary Layer Past a Sharp Cone

Simone Zuccher,^{*} Ivan Shalaev,[†] and Anatoli Tumin[‡]

University of Arizona, Tucson, Arizona 85721

and

Eli Reshotko[§]

Case Western Reserve University, Cleveland, Ohio 44106

DOI: 10.2514/1.22541

Optimal disturbances for the supersonic flow past a sharp cone are computed to assess the effects due to flow divergence. This geometry is chosen because previously published studies on compressible optimal perturbations for flat plate and sphere could not isolate the influence of divergence alone, as many factors characterized the growth of disturbances on the sphere (flow divergence, pressure gradient, centrifugal forces, and dependence of the edge parameters on the local Mach number). Flow-divergence effects result in the presence of an optimal distance from the cone tip for which the optimal gain is the largest possible, showing that divergence effects are stronger in the proximity of the cone tip. By properly rescaling the gain, wave number, and streamwise coordinate due to the fact that the boundary-layer thickness on the sharp cone is $\sqrt{3}$ thinner than the one over the flat plate, it is found that both the gain and the wave number compare fairly well. Moreover, results for the sharp cone collapse into those for the flat plate when the initial location for the computation tends to the final one and when the azimuthal wave number is very large. Results show also that a cold wall enhances transient growth.

Nomenclature

$A, B_0, B_1, B_2, C,$	= 5×5 matrices	V	= base-flow wall-normal velocity component
$D, H_1, H_2, M, \tilde{M}$		v	= perturbation wall-normal velocity component
E	= perturbation energy	w	= perturbation spanwise velocity component
\mathbf{f}	= vector of perturbation unknowns	x	= streamwise coordinate
G	= energy ratio $G = E_{\text{out}}/E_{\text{in}}$	y	= wall-normal coordinate
H	= wall-normal characteristic length	β	= spanwise wave number for flat plate
i	= $\sqrt{-1}$	γ	= specific heat ratio
\mathcal{J}	= objective function	Δx	= streamwise interval ($\Delta x = x_{\text{out}} - x_{\text{in}}$)
L	= streamwise characteristic length	ϵ	= small parameter ($\epsilon = H_{\text{ref}}/L_{\text{ref}}$)
\mathcal{L}	= augmented functional	θ	= half-angle of cone tip
M	= Mach number	ν	= kinematic viscosity
m	= azimuthal index	ρ	= density
\tilde{m}	= azimuthal wave number ($\tilde{m} = \epsilon m$)	ϕ	= azimuthal coordinate
n	= n th streamwise step		
Pr	= Prandtl number		
p	= perturbation pressure		
\mathbf{p}	= vector of adjoint variables		
Re	= Reynolds number ($Re = \frac{UL}{\nu}$)	<i>Subscript</i>	
T	= temperature	ad	= adiabatic conditions
U	= base-flow streamwise velocity component	in	= inlet conditions
u	= perturbation streamwise velocity component	loc	= local (edge) conditions
		out	= outlet conditions
		ref	= reference conditions
		s	= basic state
		w	= wall conditions
		∞	= upstream conditions
		<i>Superscript</i>	
		T	= transpose

Presented as Paper 1113 at the 44th AIAA Aerospace Sciences Meeting and Exhibit, Reno, Nevada, 9–12 January 2006; received 18 January 2006; revision received 21 September 2006; accepted for publication 30 October 2006. Copyright © 2006 by the American Institute of Aeronautics and Astronautics, Inc. All rights reserved. Copies of this paper may be made for personal or internal use, on condition that the copier pay the \$10.00 per-copy fee to the Copyright Clearance Center, Inc., 222 Rosewood Drive, Danvers, MA 01923; include the code \$10.00 in correspondence with the CCC.

^{*}Research Assistant Professor, Department of Aerospace and Mechanical Engineering. Currently at the Department of Computer Science, University of Verona, Verona, Italy. Member AIAA.

[†]Graduate Student, Department of Aerospace and Mechanical Engineering.

[‡]Professor, Department of Aerospace and Mechanical Engineering. Associate Fellow AIAA.

[§]Kent H. Smith Professor Emeritus of Engineering, Department of Mechanical and Aerospace Engineering. Fellow AIAA.

I. Introduction

IN MANY applications transition to turbulence occurs without the classical exponential growth. On the contrary, a transient growth of the disturbance energy and a subsequent downstream decay is observed in flows that are stable to wavelike perturbations such as Tollmien–Schlichting (TS) waves. The problem of optimal disturbances, in the context of bypass transition to turbulence, has been of great interest during the last decade.

Transient growth arises from the coupling between slightly damped, highly oblique Orr–Sommerfeld (OS) and Squire modes leading to algebraic growth followed by exponential decay, in subcritical regions outside the TS neutral curve. A weak transient growth can also occur for two-dimensional modes because the OS operator and its compressible counterpart are not self-adjoint, and therefore their eigenfunctions are not strictly orthogonal [1].

Historically, the first approach to nonmodal disturbances was in the inviscid limit and in the temporal framework, where it was found that the streamwise disturbance velocity amplitude may grow algebraically in time, even though the basic flow does not possess an inflection point [2]. Several other pioneering works followed [3–9] in the temporal framework, recognizing the great potential of nonmodal growth for explaining bypass transition. For a brief account on the development of transient-growth studies the reader is referred to [10].

Optimal perturbations in the spatial framework have only more recently been considered. The spatial Cauchy problem within the scope of the linearized Navier–Stokes equations is, however, radically different from the temporal one and ill posed [10,11], raising some obstacles in applying to the spatial analysis the same optimization methods used in the temporal case. The ill posedness of the spatial Cauchy problem was first overcome by considering the (linearized) boundary-layer equations [12,13] instead of the Navier–Stokes equations, and including nonparallel effects. The optimal initial disturbance was found to be composed of stationary streamwise vortices whereas the induced velocity field was dominated by streamwise streaks. In the spatial framework, optimal perturbations have also been computed in the nonlinear case [14].

In the compressible case, and within the scope of the parallel flow approximation, temporal [15,16] and spatial [17–19] analyses of the transient-growth phenomenon have been carried out. A model for transient growth including nonparallel effects in the compressible boundary layer past a flat plate has also been developed [20] and then extended to the compressible boundary layer past a sphere [10,11,19]. In [10,11] compressible optimal perturbations were calculated by including surface curvature effects and nonparallel growth of the boundary layer. Moreover, the use of a full energy norm at the inlet [10] and at the outlet [10,11] was considered, motivated by the fact that in a flowfield dominated by streamwise vortices, the wall-normal and spanwise velocity components at the outlet might also play a role in the energy norm to be maximized. This could be the case for a blunt body, for which there are some indications that the largest transient growth is located close to the stagnation point [21], where a flowfield dominated by streaks might not yet have been established.

Despite the efforts to date, some issues regarding transition in supersonic flows are still open. One of them is the long-standing blunt-body paradox [17]. At high-speed flight, boundary-layer transition on a blunt body occurs in a region that is subsonic and characterized by a favorable pressure gradient and therefore stable to TS-instability-like phenomena. Transient growth seems to be a promising mechanism to explain such a paradox [10,21]. However, the ultimate elucidation of the blunt-body paradox requires solving the roughness receptivity problem, which can explain the origin of the perturbation. The latter issue has not been addressed yet.

In the previously cited works concerning the compressible boundary layer past a sphere [10,11], several effects contribute to the results, such as the geometrical divergence of the flow, the centrifugal forces, the pressure gradient, and the indirect dependence of the edge conditions (at the edge of the boundary layer) on the Mach number through the meridional coordinate. On the contrary, the supersonic boundary layer past a flat plate does not include any of these effects. A comparison between flat-plate results and sharp-cone results, on the other hand, would shed some light on the role played by flow divergence, due to geometrical factors only. In the case of the sharp cone, in fact, there are no centrifugal forces and the Mach number is constant in the streamwise direction, excluding two out of three effects present in the compressible boundary layer past a sphere. An analysis of the optimal perturbations in the supersonic flow over a sharp cone is, however, still missing.

The objective of the present work is therefore the characterization of optimal disturbances in the supersonic boundary layer over a sharp cone. The aim is twofold. Results here obtained, when compared with the flat-plate and sphere cases, will elucidate the role played by the flow divergence alone. Secondly, the extension to the axisymmetric case of the sharp cone represents an intermediate step toward the computation of optimal perturbations in the supersonic boundary layers for more realistic geometries, such as the blunt-nose cone and three-dimensional geometries.

II. Governing Equations

The governing equations for steady, three-dimensional disturbances in the supersonic flow past a sharp cone are derived from the linearized Navier–Stokes equations, in the same fashion as in [10,11,19,20].

A small parameter $\epsilon = H_{\text{ref}}/L_{\text{ref}}$ is introduced for scaling purposes, where $H_{\text{ref}} = \sqrt{\nu_{\text{ref}} L_{\text{ref}}/U_{\text{ref}}}$ is a typical-boundary layer length in the wall-normal direction y and L_{ref} is a typical scale of the geometry (length of cone L in the present case). The scaling parameter ϵ is thus strictly related to the Reynolds number $\epsilon = Re_{\text{ref}}^{-1/2}$, where $Re_{\text{ref}} = U_{\text{ref}} L_{\text{ref}}/\nu_{\text{ref}}$ is the reference Reynolds number.

As it follows from previous works regarding optimal perturbations in both incompressible and compressible boundary layers [10,11,13,14,19,22,23], the disturbance flow is expected to be dominated by streamwise vortices and therefore the following scaling is employed [10]. The streamwise coordinate x is normalized with L_{ref} , whereas the wall-normal coordinate y is scaled with ϵL_{ref} . The azimuthal coordinate ϕ , being an angle, is not normalized. The streamwise velocity component u is scaled with U_{ref} , wall-normal velocity v and azimuthal velocity w with ϵU_{ref} , temperature T with T_{ref} , and pressure p with $\epsilon^2 \rho_{\text{ref}} U_{\text{ref}}^2$. Density ρ is eliminated through the state equation.

Because of the scaling adopted, the second derivative with respect to the streamwise coordinate x and $\partial p/\partial x$ are smaller than the other terms, and are therefore neglected. This leads to a parabolic system of equations.

Perturbations are assumed to be periodic in the azimuthal direction ϕ as $\exp(im\phi)$, where m is the azimuthal index, so that the general unknown can be expressed as $q(x, y) \exp(im\phi)$, where $q(x, y)$ is the amplitude, which depends on x and y , and i is the imaginary unit.

If the vector of perturbations is $\mathbf{f} = [u, v, w, T, p]^T$ (where the superscript T denotes the transpose), with $w = i\tilde{w}$ (\tilde{w} being the amplitude of the spanwise velocity component), the governing equations can be written as follows:

$$(\mathbf{A}\mathbf{f})_x = (\mathbf{D}\mathbf{f}_y)_x + \mathbf{B}_0\mathbf{f} + \mathbf{B}_1\mathbf{f}_y + \mathbf{B}_2\mathbf{f}_{yy} \quad (1)$$

This form of the governing equations is general and can be derived for different geometries such as flat plate, sphere, sharp cone, or blunt-nose cone. Nonzero elements of the 5×5 real matrices \mathbf{A} , \mathbf{B}_0 , \mathbf{B}_1 , \mathbf{B}_2 , and \mathbf{D} are given in the Appendix. New terms, relative to the flat-plate case, arise in the equation due to the geometrical factors introduced by the half-angle of the cone θ .

As far as boundary conditions are concerned, all perturbations are required to be zero at the wall except for p , whereas in the freestream all perturbations vanish except for v :

$$\begin{aligned} y = 0: & \quad u = 0; v = 0; w = 0; T = 0 \\ y \rightarrow \infty: & \quad u \rightarrow 0; w \rightarrow 0; p \rightarrow 0; T \rightarrow 0 \end{aligned} \quad (2)$$

To isolate the derivative with respect to x , system (1) can be recast as

$$(\mathbf{H}_1\mathbf{f})_x + \mathbf{H}_2\mathbf{f} = 0 \quad (3)$$

where operators \mathbf{H}_1 and \mathbf{H}_2 are still 5×5 real matrices and contain the dependence on x and y due to the basic flow:

$$\mathbf{H}_1 = \mathbf{A} - \mathbf{D}(\cdot)_y; \quad \mathbf{H}_2 = -\mathbf{B}_0 - \mathbf{B}_1(\cdot)_y - \mathbf{B}_2(\cdot)_{yy} \quad (4)$$

System (3) is parabolic in nature and can be solved by means of a downstream marching procedure with initial data specified at the inlet section of the domain $x = x_{in}$.

It is worth noting that the disturbance equations are not Reynolds number independent (contrary to the flat-plate case) because of the parameter ϵ in the scaling, which is associated with geometrical effects.

III. Formulation of the Optimization Problem

The problem of finding arbitrarily normalized optimal perturbations practically reduces to performing a constrained optimization. The constraints are the governing equation (3) and the normalization of the initial energy of the perturbation at the inlet, E_{in} . The objective function is a particular norm to be identified and therefore arbitrary. However, it should be a measure of the flow conditions relevant to the transition process. This choice is neither easy nor unique. In previous works dealing with optimal perturbations in the incompressible framework [12–14,22,23], the kinetic energy of the disturbance field has always been the choice.

In the compressible case, previous works [10,11,19,20] maximized Mack's energy norm [24] of the perturbation kinetic energy, density, and temperature (or simply the part containing u and T) at the outlet plane,

$$E_{out} = \int_0^\infty \left[\rho_{s_{out}} [u_{out}^2 + \epsilon^2 (v_{out}^2 + w_{out}^2)] + \frac{\rho_{out}^2 T_{s_{out}}}{\gamma \rho_{s_{out}} M^2} + \frac{T_{out}^2 \rho_{s_{out}}}{\gamma (\gamma - 1) T_{s_{out}} M^2} \right] dy \quad (5)$$

in which the scaling described in Sec. II is employed. Expression (5) was derived for perturbations developing in the boundary layer over a flat plate within the temporal framework and is here used for the spatial case, as done in [20]. After employing the equation of state for the basic flow and for the perturbation, and observing that in the limit $\epsilon \rightarrow 0$ v and w can be neglected (Reynolds-independent approach, see [13]), the norm reads

$$E_{out} = \int_0^\infty \left[\rho_{s_{out}} u_{out}^2 + \frac{\rho_{s_{out}} T_{out}^2}{(\gamma - 1) T_{s_{out}}^2 M^2} \right] dy \quad (6)$$

or more compactly

$$E_{out} = \int_0^\infty (\mathbf{f}_{out}^T \tilde{\mathbf{M}}_{out} \mathbf{f}_{out}) dy \quad (7)$$

where the linear operator $\tilde{\mathbf{M}}_{out}$ is the diagonal 5×5 matrix

$$\tilde{\mathbf{M}}_{out} = \begin{bmatrix} \rho_{s_{out}} & 0 & 0 & 0 & 0 \\ 0 & 0 & 0 & 0 & 0 \\ 0 & 0 & 0 & 0 & 0 \\ 0 & 0 & 0 & \frac{\rho_{s_{out}}}{(\gamma - 1) T_{s_{out}}^2 M^2} & 0 \\ 0 & 0 & 0 & 0 & 0 \end{bmatrix} \quad (8)$$

The initial condition for the compressible boundary-layer equations is not arbitrary, but only three of the five variables can be imposed at x_{in} [25]. However, in the incompressible case and for $Re \rightarrow \infty$, it was observed that the choice $u_{in} = 0$, $p_{in} = 0$, v_{in} and w_{in} related by the continuity equation corresponds to the maximum gain in an input–output fashion [13] (in the incompressible case the number of independent initial conditions is two; see also [13,14,26]). This choice also corresponds to the physical mechanism, observed in transitional boundary-layer flows, known as the lift-up effect [27], according to which streamwise vortices lift low momentum flow up (from the wall) and push down high momentum flow causing streaks that eventually break down to turbulence. Led by these considerations, here we focus on initial perturbations with only v and w nonzero, which correspond to steady, streamwise vortices.

The kinetic energy of the optimal disturbance \mathbf{f}_{in} , if only v_{in} and w_{in} are nonzero, is therefore

$$E_{in} = \int_0^\infty [\rho_{s_{in}} \epsilon^2 (v_{in}^2 + w_{in}^2)] dy \quad (9)$$

or more compactly

$$E_{in} = \int_0^\infty (\mathbf{f}_{in}^T \tilde{\mathbf{M}}_{in} \mathbf{f}_{in}) dy \quad (10)$$

where $\tilde{\mathbf{M}}_{in}$ is the 5×5 diagonal matrix

$$\tilde{\mathbf{M}}_{in} = \begin{bmatrix} 0 & 0 & 0 & 0 & 0 \\ 0 & \epsilon^2 \rho_{s_{in}} & 0 & 0 & 0 \\ 0 & 0 & \epsilon^2 \rho_{s_{in}} & 0 & 0 \\ 0 & 0 & 0 & 0 & 0 \\ 0 & 0 & 0 & 0 & 0 \end{bmatrix} \quad (11)$$

The quantity to be maximized is $G = E_{out}/E_{in}$, the ratio between the outlet and the inlet norms. However, to allow direct comparison with previous works, $G\epsilon^2$ will be presented in the Results section

$$G\epsilon^2 = \frac{\int_0^\infty \left[\rho_{s_{out}} u_{out}^2 + \frac{\rho_{s_{out}} T_{out}^2}{(\gamma - 1) T_{s_{out}}^2 M^2} \right] dy}{\int_0^\infty [\rho_{s_{in}} (v_{in}^2 + w_{in}^2)] dy} \quad (12)$$

Because the problem is linear, an arbitrary normalization for the initial disturbance at x_{in} can be chosen, for example, $E_{in} = 1$, so that the maximization of Eq. (12) turns out to be equivalent to the maximization of expression (7), that is, $\mathcal{J} = E_{out}$.

It should be clear now that the whole problem of finding optimal perturbations reduces to a constrained optimization, in which we seek the initial conditions for the disturbance equation (3) that maximize Eq. (7) and that satisfy the constraint $E_{in} = E_0$ at x_{in} , together with the direct equation (3) and boundary conditions (2) at each $x \in (x_{in}; x_{out})$.

The details of the constrained optimization procedure are not reported here, as they can be found in [10,11], to which the reader is referred. The classical Lagrange multiplier technique is applied to the discrete version of problem (3), which can be recast as $\mathbf{C}_{n+1} \mathbf{f}_{n+1} = \mathbf{B}_n \mathbf{f}_n$, leading to the so-called adjoint equations [10,11,13,14,22,23,26,28] (here n denotes the n th grid node in the streamwise direction x , \mathbf{f} is the vector of $5 \times N_y$ unknowns at each n station, N_y being the number of grid nodes in the wall-normal direction y ; matrices \mathbf{C} and \mathbf{B} depend on x and y , as the basic flow does, and account for the discretization in both x and y).

The use of the discrete approach has several advantages among which the necessity of an ‘‘ad hoc’’ adjoint code is avoided and a foolproof test is available by comparing the results of the direct and adjoint calculation, which must match up to machine accuracy for any step size and not only in the limit of step size tending to zero [13,14,26].

The augmented functional \mathcal{L} contains the objective function $\mathcal{J} = E_{out}$, the constraints (3) and $E_{in} = E_0$, and the Lagrange multipliers [10,11]. The optimization imposes $\delta \mathcal{L} = 0$, which leads to the adjoint equations in the discrete form and coupling conditions between the direct and adjoint problems at the inlet (x_{in}) and outlet (x_{out}). These conditions can be written in a matrix form so that their application becomes straightforward. To retrieve the outlet conditions, a system needs to be solved where the coefficient matrix is singular (due to $\partial p / \partial x = 0$ in this approximation), reflecting the fact that at least one out of five adjoint variables is free at $x = x_{out}$ and therefore can be chosen arbitrarily. For the sake of simplicity, we set the fifth adjoint variable equal to zero.

The constrained optimization formulation requires the simultaneous solution of a large, coupled system of direct equations, adjoint equations, boundary conditions, and coupling conditions. Instead of doing it in one shot, however, we employ the intrinsic parabolic nature of the equations to efficiently solve separately the two coupled problems. Such an algorithm can be outlined in the following few steps. 1) A guessed initial condition $\mathbf{f}_{in}^{(0)}$ is provided at the beginning of the optimization procedure; 2) the forward problem is solved at the i th iteration with the initial condition $\mathbf{f}_{in}^{(i)}$; 3) the objective function

$\mathcal{J}^{(i)} = E_{\text{out}}^{(i)}$ is computed at the end of the forward iteration and compared to the objective function $\mathcal{J}^{(i-1)} = E_{\text{out}}^{(i-1)}$ at the end of the previous forward iteration. If $|\mathcal{J}^{(i)}/\mathcal{J}^{(i-1)} - 1| < \epsilon_t$ (where ϵ_t is the maximum tolerance accepted to stop the optimization) then the optimization is considered converged and the problem solved; 4) if $|\mathcal{J}^{(i)}/\mathcal{J}^{(i-1)} - 1| > \epsilon_t$ the initial conditions for the backward problem are assigned at the outlet and derived from the direct solution at $x = x_{\text{out}}$; 5) the backward problem is solved from $x = x_{\text{out}}$ to $x = x_{\text{in}}$; 6) a new initial condition for the forward problem $\mathbf{f}_{\text{in}}^{(i+1)}$ is obtained from the solution of the backward problem at $x = x_{\text{in}}$ employing the coupling condition at the inlet; 7) the loop is repeated from step 2 on until it is eventually ended in step 3. It should be noted that this procedure does not necessarily guarantee convergence. If there is an attractor for the solution, then the procedure will capture it and this happens quite fast (2–3 forward–backward iterations).

IV. Discretization

A finite difference discretization scheme has been implemented to numerically solve Eq. (3) with boundary conditions (2). For the sake of generality, grid nodes in x and y are not necessarily equally spaced. A staggered grid is introduced in the wall-normal direction, with variables u , v , w , and T known at the grid nodes, and p known at the midgrid (staggered) nodes. All equations are satisfied at the grid nodes except for continuity, which is satisfied in the midgrid nodes. The use of the uneven grid in y allows us to cluster more nodes close to the wall so as to take into account the larger gradients of boundary-layer quantities in this region. The last node of the y grid is located far enough from the wall to allow satisfaction there of the boundary conditions for $y \rightarrow \infty$.

Fourth-order noncompact finite differences are used for the y discretization, employing six nodes so as to allow fourth order accuracy for the second derivative. By using six nodes, the first derivative is automatically fifth order accurate and the function (when interpolated due to the staggered grid) is sixth order accurate.

Also the discretization in the streamwise direction is based on an uneven grid. Because the system of boundary-layer equations is parabolic, a second order backward discretization is chosen, which requires the solution at two previous steps to be known. For the first step, however, a first order scheme is used because only the initial condition is available.

For further details and for a thorough derivation of the discrete adjoint equations, the reader is referred to [10,11].

V. Results

The basic flow for the sharp cone is obtained from the flat-plate case by rescaling the wall-normal coordinate y and its derivatives according to Mangler's transformation [29]. The local Mach number, M_{loc} , at the edge of the boundary layer was calculated assuming calorically perfect gas flow at freestream Mach number $M_{\infty} = 6$. Because the shock wave is assumed to be far away from the boundary layer (and perturbation), their mutual interaction is not considered. The calculations are performed for cone half-angles of $\theta = 15$ and 25 deg. The main goal in the presentation of the results is to discuss the effects originating from flow divergence induced by the geometry. The boundary-layer edge velocity, density, temperature, and viscosity at $x = L_{\text{ref}}$ are chosen as the reference parameters. All results are obtained at $\epsilon = 0.001$ unless otherwise stated.

Figure 1 shows the objective function Ge^2 obtained from the optimization procedure for $\theta = 15$ deg. Adiabatic boundary conditions are used for the temperature at the wall, $T_w/T_{\text{ad}} = 1$, and the initial station is kept constant, $x_{\text{in}} = 0.2$, while changing the outlet station. Results show that there exists a location, downstream of $x_{\text{in}} = 0.2$, where the curve of the maximum energy growth as a function of the modified azimuthal wave number, $\tilde{m} = \epsilon m$, reaches the largest value, after which the maximum of the curve decreases with increasing x_{out} . Among the computed curves, this maximum seems to be reached for $x_{\text{out}} = 0.3$. However, a better estimate can be obtained by performing a parabolic interpolation of the data corresponding to the maxima for the three cases $x_{\text{out}} = 0.275$,

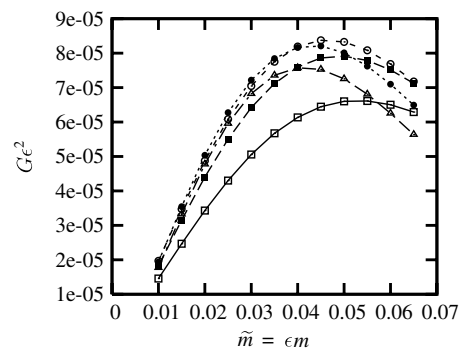


Fig. 1 Objective function Ge^2 : effect of x_{out} and \tilde{m} for $\theta = 15$ deg, $M_{\infty} = 6$, $M_{\text{loc}} = 4.37$, $T_w/T_{\text{ad}} = 1$, $x_{\text{in}} = 0.2$. □: $x_{\text{out}} = 0.25$; ■: $x_{\text{out}} = 0.275$; ○: $x_{\text{out}} = 0.3$; ●: $x_{\text{out}} = 0.35$; △: $x_{\text{out}} = 0.4$.

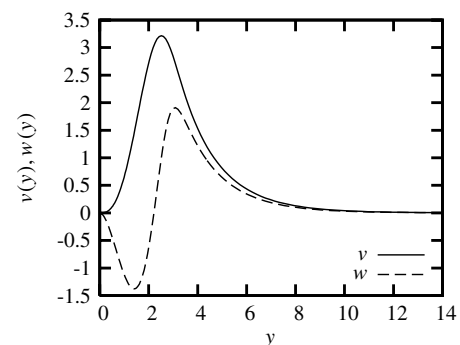


Fig. 2 Optimal perturbation at x_{in} for $\theta = 15$ deg, $M_{\infty} = 6$, $M_{\text{loc}} = 4.37$, $T_w/T_{\text{ad}} = 1$, $x_{\text{in}} = 0.2$, $x_{\text{out}} = 0.3$, and $\tilde{m} = 0.045$.

$x_{\text{out}} = 0.3$, and $x_{\text{out}} = 0.35$. This leads to the optimal outlet location $x_{\text{out}} = 0.32$, from which the optimal interval $\Delta x = x_{\text{out}} - x_{\text{in}} = 0.12$ is obtained.

The shape of the optimal perturbation at x_{in} is very similar to what has been found so far in both incompressible and compressible studies [13,20] and is shown in Fig. 2 for the largest gain observed in the previous figure, that is, $\tilde{m} = 0.045$ and $x_{\text{out}} = 0.3$. The maximum energy growth is determined by streamwise vortices generated by v and w perturbations that extend outside the boundary layer and decay at the same rate as a function of y . This type of perturbation is consistent with the assumptions employed in the scaling process.

By moving the inlet location further downstream to $x_{\text{in}} = 0.4$, results qualitatively similar to those shown in Fig. 1 are found. The corresponding estimated x_{out} that causes the maximum gain is $x_{\text{out}} = 0.64$ and the interval $\Delta x = x_{\text{out}} - x_{\text{in}} = 0.24$ is greater than the value $\Delta x = 0.12$ previously observed for $x_{\text{in}} = 0.2$. The conclusion is that divergence effects are stronger in the proximity of $x_{\text{in}} = 0$, as one could argue from geometrical considerations.

Figure 3 shows the objective function Ge^2 computed for a larger cone half-angle, $\theta = 25$ deg, while keeping $x_{\text{in}} = 0.2$ fixed. The

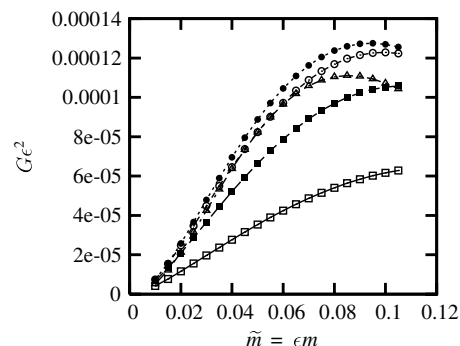


Fig. 3 Objective function Ge^2 : effect of x_{out} and \tilde{m} for $\theta = 25$ deg, $M_{\infty} = 6$, $M_{\text{loc}} = 3.22$, $T_w/T_{\text{ad}} = 1$, $x_{\text{in}} = 0.2$. □: $x_{\text{out}} = 0.225$; ■: $x_{\text{out}} = 0.25$; ○: $x_{\text{out}} = 0.275$; ●: $x_{\text{out}} = 0.3$; △: $x_{\text{out}} = 0.4$.

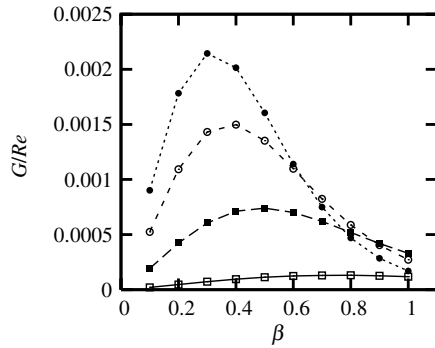


Fig. 4 Objective function G/Re , flat plate: effect of x_{out} and β for $M = 3.22$, $T_w/T_{ad} = 1$, $x_{in} = 0.4$. \square : $x_{out} = 0.45$; \blacksquare : $x_{out} = 0.6$; \circ : $x_{out} = 0.8$; \bullet : $x_{out} = 1.0$.

general trend of the results is as in Fig. 1. The estimated value of x_{out} that causes the maximum gain is $x_{out} = 0.32$, leading to $\Delta x = 0.12$. Remarkably, the latter is the same as for $\theta = 15$ deg and $x_{in} = 0.2$.

By moving the inlet location to $x_{in} = 0.4$ (for $\theta = 25$ deg), the optimal estimated outlet location is $x_{out} = 0.64$ and thus $\Delta x = 0.24$, that is, the same as for $\theta = 15$ deg. This suggests the possible insensitivity of $\Delta x = x_{out} - x_{in}$ to the nose-tip angle. However, as can be deduced by comparing Figs. 1 and 3, θ influences the values of $G\epsilon^2$, which are consistently higher for larger cone half-angles.

As opposed to the sharp-cone geometry, the flat-plate case has no effects due to the flow divergence. Therefore, by analyzing the results from the previous figures together with those obtained in the same fashion for the flat plate, more insights can be gained regarding the influence of the geometry. This is done in Fig. 4, where flat-plate results are shown for $M = 3.22$ (the local Mach number corresponding to the 25 deg cone), adiabatic wall, and $x_{in} = 0.4$. It is clear that moving the outlet location downstream leads to a monotonic increase in the curve of maximum energy growth. A precise optimal outlet x_{out} , however, is not found. This is a new finding with respect to previous figures and to previously published results for the flat plate [20], in which only the inlet location x_{in} was changed, while keeping $x_{out} = 1.0$. The straightforward conclusion from the comparison between Fig. 4 and the previous ones is that, once the inlet location is fixed, divergence effects result in the existence of an optimal outlet location $x_{out} < 1$ for which the largest energy growth is reached. This behavior was also present in the sphere case [10,11,19], corroborating the conjecture of being due to the flow divergence only.

Figure 5 plots the reverse case to what was seen before. The gain $G\epsilon^2$ is shown for the sharp-cone geometry, keeping the outlet fixed, $x_{out} = 1.0$, and changing the inlet x_{in} , for $\theta = 25$ deg (the other parameters are $M_\infty = 6$, $M_{loc} = 3.22$, and $T_w/T_{ad} = 1$). An optimal inlet location is now found. By performing the same type of parabolic interpolation for the maxima as done before, the largest energy growth is obtained for an estimated $x_{in} = 0.72$, that is, for $\Delta x = 0.28$. The latter is comparable with the value of Δx found for $x_{in} = 0.4$ while changing x_{out} for the 25 deg cone.

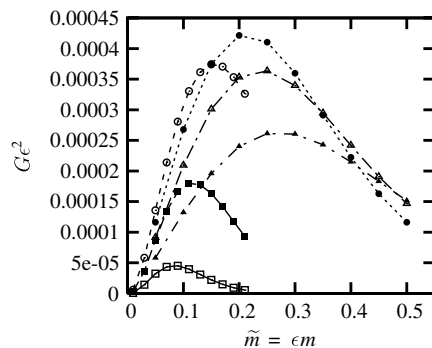


Fig. 5 Objective function $G\epsilon^2$: effect of x_{in} and \tilde{m} for $\theta = 25$ deg, $M_\infty = 6$, $M_{loc} = 3.22$, $T_w/T_{ad} = 1$, $x_{out} = 1.0$. \square : $x_{in} = 0.2$; \blacksquare : $x_{in} = 0.4$; \circ : $x_{in} = 0.6$; \bullet : $x_{in} = 0.8$; \blacktriangle : $x_{in} = 0.9$.

VI. Quantitative Comparison Between Flat-Plate and Sharp-Cone Results

Results presented in Fig. 4 certainly shed a new light on the differences between flat-plate and sharp-cone geometries that can be attributed to flow divergence. However, the order of magnitude of the gain reported in that figure differs quite remarkably from what is shown in the figures for the sharp cone. This allows only a qualitative comparison. To compare quantitatively the energy growth for the flat plate and cone, both physics and scaling should be considered.

The physics suggests that the results for the sharp cone should reduce to those obtained for the flat plate in the limits $x_{in} \rightarrow x_{out}$ and $m \rightarrow \infty$. The first is dictated by the fact that divergence effects (which are the main difference between sharp-cone and flat-plate geometries) are negligible far from the cone tip (in the proximity of x_{out}). The second limit is due to the fact that the presence of many vortices in the azimuthal direction forces the flow to be less sensitive to divergence and, thus, to behave as in the flat-plate case. To emphasize the effects of divergence in the flow past the sharp cone, therefore, we focus on the limits $x_{in} \rightarrow x_{out}$ and $m \rightarrow \infty$. The outlet location $x_{out} = 1$ is kept constant, as for the flat-plate case, so as to allow direct comparison.

The scaling is important as well. The fact that the boundary-layer thickness over the cone is $1/\sqrt{3}$ times that of the boundary-layer thickness over the flat plate, and the same length scale L_{ref} is used in the definition of the Reynolds number in both cases, suggests that G/Re for the flat plate [10,11,20] must be compared with $3G\epsilon^2$. On the other hand, the wave number $\beta z/H_{ref\ plate}$ must be compared with

$$m\phi = \frac{mz}{R} = \frac{mH_{ref\ cone}}{R} \frac{z}{H_{ref\ cone}}$$

where z is the transverse coordinate along the cone surface and R is the local radius. The comparison between $\beta z/H_{ref\ plate}$ and $m\phi$, therefore, reduces to the comparison between β and $mH_{ref\ cone}/R$. However, because $H_{ref\ cone} = H_{ref\ plate}/\sqrt{3}$ and $R = L_{ref} \sin \theta$, by taking into account that $\epsilon = H_{ref\ plate}/L_{ref}$, one gets

$$\frac{mH_{ref\ cone}}{R} = \frac{mH_{ref\ plate}}{\sqrt{3}R} = \frac{mH_{ref\ plate}}{\sqrt{3}L \sin \theta} = \frac{m\epsilon}{\sqrt{3} \sin \theta} = \frac{\tilde{m}}{\sqrt{3} \sin \theta}$$

This rescaling is employed in Fig. 6 for the sharp-cone results to compare them with those for the flat plate. Many conclusions can be deduced from these plots, obtained by changing θ and $\Delta x = x_{out} - x_{in}$. First, the scaling is correct in that all the results for the cone with $x_{in} = 0.95$ and $x_{out} = 1.0$ (\square , \triangle , ∇ , \diamond) collapse onto one curve, regardless of θ . Secondly, ϵ does not have any effect on the gain function ($3G\epsilon^2$), as is proved by comparison of the cases for $\epsilon = 0.001$ (\square) and $\epsilon = 0.0001$ (\triangle), both referring to $x_{in} = 0.95$, $x_{out} = 1.0$, and $\theta = 15$ deg. Third, the comparison between the cone (empty symbols) and the flat plate (full symbols) should be carried

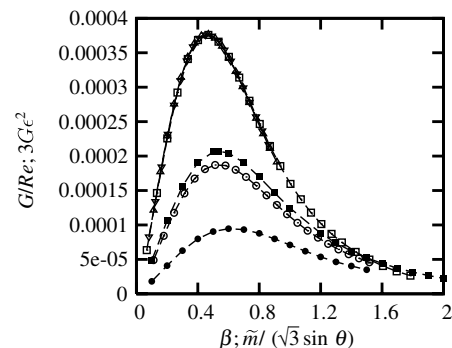


Fig. 6 Objective function, comparison between G/Re (flat plate) and $3G\epsilon^2$ (sharp cone) as a function of β and $\tilde{m}/(\sqrt{3} \sin \theta)$, respectively, effect of x_{in} and wave number. $M_{loc} = 3$, $T_w/T_{ad} = 1$, $x_{out} = 1.0$. \square : $\theta = 15$ deg and $x_{in} = 0.95$; \triangle : $\theta = 15$ deg, $x_{in} = 0.95$ and $\epsilon = 0.0001$; \circ : $\theta = 15$ deg and $x_{in} = 0.97113$; ∇ : $\theta = 25$ deg and $x_{in} = 0.95$; \blacksquare : flat plate, $x_{in} = 0.913$; \bullet : flat plate, $x_{in} = 0.95$.

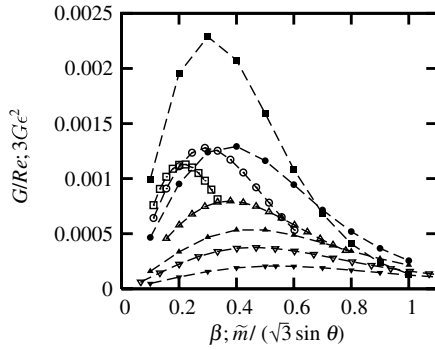


Fig. 7 Objective function, comparison between G/Re (flat plate, full symbols) and $3G\epsilon^2$ (sharp cone, empty symbols) as a function of β and $\tilde{m}/(\sqrt{3} \sin \theta)$, respectively, effect of x_{in} and wave number. $M_{loc} = 3$, $T_w/T_{ad} = 1$, $x_{out} = 1.0$. Sharp cone, \square : $\theta = 15$ deg and $x_{in} = 0.6$; \circ : $\theta = 15$ deg and $x_{in} = 0.8$; \triangle : $\theta = 15$ deg and $x_{in} = 0.9$; ∇ : $\theta = 15$ deg and $x_{in} = 0.95$. Flat plate, \blacksquare : $x_{in} = 0.30718$; \bullet : $x_{in} = 0.65359$, \blacktriangle : $x_{in} = 0.82679$, \blacktriangledown : $x_{in} = 0.913$.

out with further care with respect to Δx . In fact, because of the difference in the boundary-layer thickness between the flat plate and the cone, distances Δx having about the same number of boundary-layer thicknesses should be considered. We suggest comparing Δx_{cone} with $\Delta x_{plate}/\sqrt{3}$, implying that the sharp-cone cases $x \in [0.95; 1]$ and $x \in [0.97113; 1]$ should be compared, respectively, with the flat-plate cases $x \in [0.913; 1]$, and $x \in [0.95; 1]$. Figure 6 confirms this by showing that results for the sharp cone and the flat plate collapse onto each other for $\tilde{m} \rightarrow \infty$, when the correct intervals Δx are considered (see \square vs \blacksquare and \circ vs \bullet).

To investigate the intuitive idea that the difference in the energy growth between the two geometries should diminish as $x_{in} \rightarrow x_{out}$ and $m \rightarrow \infty$, in Fig. 7 we compare the sharp cone (empty symbols), $\theta = 15$ deg, and the flat plate (full symbols) at different x_{in} . The parameter Δx is properly rescaled so that \square compares with \blacksquare , \circ with \bullet , \triangle with \blacktriangle , and ∇ with \blacktriangledown . Results confirm what is expected (see, for example, the sharp-cone case $x_{in} = 0.95$, ∇ , compared to the flat-plate case $x_{in} = 0.913$, \blacktriangledown).

Having the correct scaling, further comparisons between the two geometries can be carried out. The effect of wall temperature, which can either promote or delay transition in supersonic boundary layers, is shown in Fig. 8 in the limit $x_{in} \rightarrow x_{out}$. Empty symbols refer to the sharp cone ($\theta = 15$ deg) and full symbols to the flat plate. It can be noted that a cold wall, that is, $T_w/T_{ad} = 0.5$ (\circ and ∇ for the sharp cone, corresponding to the cases \bullet and \blacktriangledown for the flat plate) enhances the energy growth, as already pointed out in previous studies [10,11,19,20]. Moreover, not only is the gain larger for a cold wall,

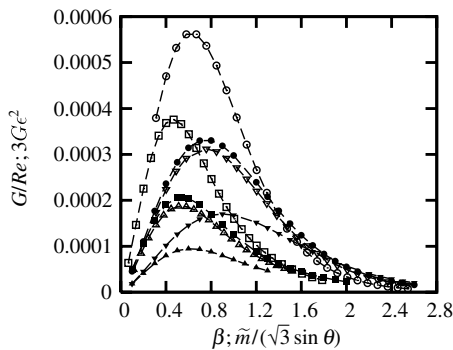


Fig. 8 Objective function, comparison between G/Re (flat plate, full symbols) and $3G\epsilon^2$ (sharp cone, empty symbols) as a function of β and $\tilde{m}/(\sqrt{3} \sin \theta)$, respectively, effect of x_{in} and wave number and T_w/T_{ad} . $M_{loc} = 3$, $x_{out} = 1.0$. Sharp cone, \square : $\theta = 15$ deg, $T_w/T_{ad} = 1.0$ and $x_{in} = 0.95$; \circ : $\theta = 15$ deg, $T_w/T_{ad} = 0.5$ and $x_{in} = 0.95$; \triangle : $\theta = 15$ deg, $T_w/T_{ad} = 1.0$ and $x_{in} = 0.97113$; ∇ : $\theta = 15$ deg, $T_w/T_{ad} = 0.5$ and $x_{in} = 0.97113$. Flat plate, \blacksquare : $x_{in} = 0.913$ and $T_w/T_{ad} = 1.0$; \bullet : $x_{in} = 0.913$ and $T_w/T_{ad} = 0.5$; \blacktriangle : $x_{in} = 0.95$ and $T_w/T_{ad} = 1.0$; \blacktriangledown : $x_{in} = 0.95$ and $T_w/T_{ad} = 0.5$.

but the wave number for which the optimum is reached is also larger. For very large values of the wave number, results for the two geometries collapse onto each other, as a consequence of the $m \rightarrow \infty$ limit previously described. This behavior is consistent, for every case considered (see also \square vs \blacksquare , and ∇ vs \blacktriangledown).

All considered examples demonstrate that the growth factor G for the flat plate is larger than that for the cone leading to the conclusion that flow divergence has an abilizing effect.

VII. Conclusions

Optimal disturbances originating in the supersonic boundary-layer flow past a sharp axisymmetric cone have been studied, motivated by several factors. Similar studies previously published [10,11,19,20] reported optimal perturbations for a flat plate and sphere, but a direct comparison between them was complicated by the many effects present in the case of the sphere (flow divergence, pressure gradient, centrifugal forces, and dependence of the edge parameters on the local Mach number). The sharp-cone geometry, on the other hand, is simpler than the spherical one and characterized by flow-divergence effects only, allowing us to identify them more easily when comparing a flat plate, a sharp cone, and a sphere. Moreover, in the development of the studies toward a more realistic three-dimensional supersonic case, the sharp-cone geometry is a natural step before the blunt-nose cone.

Equations are obtained from the linearized Navier–Stokes equations by employing a scaling that assumes the perturbation dominated by streamwise vortices. This leads to parabolic-in- x equations. The optimization is carried out in an iterative manner, relying on the alternate solution of the direct and adjoint problems related by coupling conditions at the inlet and outlet.

A first set of results, obtained by keeping the inlet location fixed and changing the outlet location, provides interesting conclusions on flow divergence. An optimal distance Δx from the inlet ($\Delta x = x_{out} - x_{in}$) is found at $x_{out} < 1$, for which the curve of the maximum gain is the largest. The increase of Δx when the inlet location is moved downstream suggests that divergence effects are stronger in the proximity of the cone tip. On the other hand, increasing the cone half-angle does not seem to affect Δx . When these results are compared with the flat-plate case, it becomes clear that the presence of an optimal downstream location for the energy growth is a unique characteristic of flows dominated by geometrical divergence, such as those on sharp cones and spheres. For the case of the flat plate, in fact, for a given inlet station x_{in} , the curve of optimal energy gain reaches larger values monotonically as the outlet location, x_{out} , is moved downstream.

A second set of results is obtained by keeping the outlet location fixed and changing the inlet location. The gain, wave number, and Δx are properly rescaled taking into account the half-cone angle θ and the fact that the boundary-layer thickness on the sharp cone is $\sqrt{3}$ thinner than that over the flat plate. By comparing the two geometries, it is found that both the gain and the wave number scale fairly well and that results for the sharp cone collapse onto those for the flat plate in the limits $x_{in} \rightarrow x_{out}$ and $m \rightarrow \infty$.

Comparisons of growth factors for cones and flat plates demonstrate that the flow divergence has a stabilizing effect on transient growth. Results confirm also that a cold wall enhances transient growth.

Appendix: Matrices for Compressible Flow Past a Sharp Cone

Assuming that the basic flow is known, let x , y , and ϕ denote the three independent coordinates, where x is the streamwise distance from the nose tip, y the wall-normal distance, and ϕ the azimuthal angle. With this notation, u , v , and w are the corresponding velocity field, that together with temperature T and pressure p form the set of the problem's unknowns. Density ρ is related to T and p by the state equation and thus is not an explicit unknown.

The scaling is as described in Sec. II. The unknowns in the disturbance equations are only five and are assumed to be

proportional to $\exp(im\phi)$, where m is the azimuthal index and i the imaginary unit.

In what follows viscosity μ_s is assumed to be a function of temperature only, and therefore μ'_s stands for the derivative $d\mu_s/dT_s$.

Transformations of the linearized equations lead to the system of partial differential equations

$$(\mathbf{A}\mathbf{f})_x = (\mathbf{D}\mathbf{f}_y)_x + \mathbf{B}_0\mathbf{f} + \mathbf{B}_1\mathbf{f}_y + \mathbf{B}_2\mathbf{f}_{yy} \quad (\text{A1})$$

where \mathbf{A} , \mathbf{B}_0 , \mathbf{B}_1 , \mathbf{B}_2 , and \mathbf{D} are 5×5 matrices, and can be recast as

$$(\mathbf{H}_1\mathbf{f})_x + \mathbf{H}_2\mathbf{f} = 0 \quad (\text{A2})$$

Operators \mathbf{H}_1 and \mathbf{H}_2 are still 5×5 matrices and contain the dependence on x and y :

$$\mathbf{H}_1 = \mathbf{A} - \mathbf{D}(\cdot)_y; \quad \mathbf{H}_2 = -\mathbf{B}_0 - \mathbf{B}_1(\cdot)_y - \mathbf{B}_2(\cdot)_{yy} \quad (\text{A3})$$

The expression to be maximized, in the limit $\epsilon \rightarrow 0$ (i.e., $Re \rightarrow \infty$), is the integral in the wall-normal direction of the kinetic energy and temperature. After the transformations imposed by the geometry, E_{out} reads

$$E_{\text{out}} = \int_0^\infty \sin \theta(x + \epsilon y \cot \theta) \left[\rho_{s,\text{out}} u_{\text{out}}^2 + \frac{\rho_{s,\text{out}} T_{s,\text{out}}^2}{(\gamma - 1) T_{s,\text{out}}^2 M^2} \right] dy \quad (\text{A4})$$

where the term $\sin \theta(x + \epsilon y \cot \theta)$ stems from the integration over the whole domain, that is, over the three independent variables.

The nonzero elements of the matrices are here reported, with the wave number β defined as $\beta = \tilde{m}/(x + \epsilon y \cot \theta)$, \tilde{m} being $\tilde{m} = \epsilon m$.

Continuity equation:

$$A^{11} = \rho_s; \quad A^{14} = -\frac{\rho_s U_s}{T_s}; \quad B_0^{11} = -\frac{\rho_s}{(x + \epsilon y \cot \theta)};$$

$$B_0^{12} = -\frac{\partial \rho_s}{\partial y}; \quad B_0^{13} = -\beta \rho_s;$$

$$B_0^{14} = \frac{\partial}{\partial y} \left(\frac{\rho_s V_s}{T_s} \right) + \frac{\rho_s U_s}{T_s(x + \epsilon y \cot \theta)}; \quad B_1^{13} = -\rho_s;$$

$$B_1^{14} = \frac{\rho_s V_s}{T_s}$$

x -momentum equation:

$$A^{21} = 2\rho_s U_s; \quad A^{24} = -\frac{\rho_s U_s^2}{T_s};$$

$$B_0^{21} = -\frac{\partial \rho_s V_s}{\partial y} - \mu_s \beta^2 - \frac{2\rho_s U_s}{(x + \epsilon y \cot \theta)}; \quad B_0^{22} = -\frac{\partial \rho_s U_s}{\partial y};$$

$$B_0^{23} = -\beta \rho_s U_s;$$

$$B_0^{24} = \frac{\partial}{\partial y} \left(\frac{\rho_s V_s U_s}{T_s} \right) + \frac{\partial}{\partial y} \left(\mu'_s \frac{\partial U_s}{\partial y} \right) + \frac{\rho_s U_s^2}{T_s(x + \epsilon y \cot \theta)};$$

$$B_1^{21} = \frac{\partial \mu_s}{\partial y} - \rho_s V_s; \quad B_1^{22} = -\rho_s U_s;$$

$$B_1^{24} = \frac{\rho_s U_s V_s}{T_s} + \mu'_s \frac{\partial U_s}{\partial y}; \quad B_2^{21} = \mu_s$$

y -momentum equation:

$$A^{31} = \rho_s V_s + \frac{2}{3} \frac{\partial \mu_s}{\partial y}; \quad A^{32} = \rho_s U_s;$$

$$A^{34} = -\frac{\rho_s U_s V_s}{T_s} - \mu'_s \frac{\partial U_s}{\partial y};$$

$$B_0^{31} = \frac{2}{3} \frac{\partial}{\partial x} \left(\frac{\partial \mu_s}{\partial y} \right) + \frac{1}{(x + \epsilon y \cot \theta)} \left(-\frac{2}{3} \frac{\partial \mu_s}{\partial y} - \rho_s V_s \right);$$

$$B_0^{32} = -2 \frac{\partial \rho_s V_s}{\partial y} - \beta^2 \mu_s - \frac{\rho_s U_s}{(x + \epsilon y \cot \theta)};$$

$$B_0^{33} = -\beta \rho_s V_s - \frac{2\beta}{3} \frac{\partial \mu_s}{\partial y};$$

$$B_0^{34} = \frac{1}{(x + \epsilon y \cot \theta)} \left[\frac{\rho_s U_s V_s}{T_s} + \frac{1}{3} \mu'_s \frac{\partial U_s}{\partial y} - \frac{2}{3} U_s \frac{\partial \mu'_s}{\partial y} \right] + \frac{\partial}{\partial y} \left(\frac{\rho_s V_s^2}{T_s} \right) + \frac{\partial \mu'_s}{\partial y} \left[\frac{4}{3} \frac{\partial V_s}{\partial y} - \frac{2}{3} \frac{\partial U_s}{\partial x} \right] + \mu'_s \left[-\frac{\partial}{\partial x} \left(\frac{\partial U_s}{\partial y} \right) + \frac{4}{3} \frac{\partial^2 V_s}{\partial y^2} + \frac{1}{3} \frac{\partial^2 U_s}{\partial x \partial y} \right];$$

$$B_1^{31} = \frac{\mu_s}{3(x + \epsilon y \cot \theta)} + \frac{2}{3} \frac{\partial \mu_s}{\partial x}; \quad B_1^{32} = -2\rho_s V_s + \frac{4}{3} \frac{\partial \mu_s}{\partial y};$$

$$B_1^{33} = \frac{\beta \mu_s}{3};$$

$$B_1^{34} = \mu'_s \left[\frac{4}{3} \frac{\partial V_s}{\partial y} - \frac{2}{3} \frac{\partial U_s}{\partial x} \right] + \frac{\rho_s V_s^2}{T_s} - \frac{2U_s}{3(x + \epsilon y \cot \theta)} \mu'_s;$$

$$B_1^{35} = -1; \quad B_2^{32} = \frac{4}{3} \mu_s; \quad D^{31} = \frac{\mu_s}{3}$$

ϕ -momentum equation:

$$A^{43} = \rho_s U_s; \quad A^{44} = \frac{\mu_s \beta U_s}{3T_s};$$

$$B_0^{41} = \frac{\mu_s \beta \partial \rho_s}{3\rho_s \partial x} - \beta \frac{\partial \mu_s}{\partial x} - \frac{2\beta \mu_s}{(x + \epsilon y \cot \theta)};$$

$$B_0^{42} = \frac{\mu_s \beta \partial \rho_s}{3\rho_s \partial y} - \beta \frac{\partial \mu_s}{\partial y};$$

$$B_0^{43} = -\beta^2 \mu_s - \frac{\partial \rho_s V_s}{\partial y} - \frac{2\rho_s U_s}{(x + \epsilon y \cot \theta)};$$

$$B_0^{44} = -\frac{\beta \mu_s}{3\rho_s} \frac{\partial}{\partial y} \left(\frac{\rho_s V_s}{T_s} \right) + \frac{\rho_s U_s \beta}{3T_s} \frac{\partial}{\partial x} \left(\frac{\mu_s}{\rho_s} \right) - \frac{\mu_s U_s \beta}{3T_s(x + \epsilon y \cot \theta)} + \frac{2\beta \mu'_s \partial U_s}{3 \partial x} + \frac{2\beta \mu'_s \partial V_s}{3 \partial x} - \frac{4\beta U_s \mu'_s}{3(x + \epsilon y \cot \theta)};$$

$$B_0^{45} = \beta; \quad B_1^{43} = -\rho_s V_s + \frac{\partial \mu_s}{\partial y}; \quad B_1^{44} = -\frac{\beta \mu_s V_s}{3T_s};$$

$$B_2^{43} = \mu_s$$

Energy equation:

$$A^{51} = \rho_s T_s; \quad B_0^{51} = \frac{\gamma - 1}{\gamma} \frac{\partial p_s}{\partial x} - \frac{\rho_s T_s}{(x + \epsilon y \cot \theta)};$$

$$B_0^{52} = -\frac{\partial \rho_s T_s}{\partial y}; \quad B_0^{53} = -\beta \rho_s T_s;$$

$$B_0^{54} = \mu'_s (\gamma - 1) M_{\text{ref}}^2 \left(\frac{\partial U_s}{\partial y} \right)^2 - \frac{\beta^2 \mu_s}{Pr} + \frac{1}{Pr} \frac{\partial}{\partial y} \left(\mu'_s \frac{\partial T_s}{\partial y} \right);$$

$$B_1^{51} = 2(\gamma - 1) M_{\text{ref}}^2 \mu_s \frac{\partial U_s}{\partial y}; \quad B_1^{52} = -\rho_s T_s;$$

$$B_1^{54} = \frac{2}{Pr} \frac{\partial \mu_s}{\partial y}; \quad B_2^{54} = \frac{\mu_s}{Pr}$$

Acknowledgment

Support of this work by the U.S. Air Force Office of Scientific Research is gratefully acknowledged.

References

- [1] Reshotko, E., "Transient Growth: A Factor in Bypass Transition," *Physics of Fluids*, Vol. 13, No. 5, 2001, pp. 1067–1075.
- [2] Ellingsen, T., and Palm, E., "Stability of Linear Flow," *Physics of Fluids*, Vol. 18, No. 4, 1975, pp. 487–488.
- [3] Hultgren, L. S., and Gustavsson, L. H., "Algebraic Growth of Disturbances in a Laminar Boundary Layer," *Physics of Fluids*, Vol. 24, No. 6, 1981, pp. 1000–1004.
- [4] Farrell, B., "Optimal Excitation of Perturbations in Viscous Shear Flow," *Physics of Fluids*, Vol. 31, No. 8, 1988, pp. 2093–2102.
- [5] Boberg, L., and Brosa, U., "Onset of Turbulence in a Pipe," *Zeitschrift für Naturforschung*, Vol. 43a, No. 8–9, 1988, pp. 697–726.
- [6] Butler, K. M., and Farrell, B., "Three-Dimensional Optimal Perturbations in Viscous Shear Flow," *Physics of Fluids A*, Vol. 4, No. 8, 1992, pp. 1637–1650.
- [7] Gustavsson, L. H., "Energy Growth of Three-Dimensional Disturbances in Plane Poiseuille Flow," *Journal of Fluid Mechanics*, Vol. 224, March 1991, pp. 241–260.
- [8] Reddy, S. C., and Henningson, D. S., "Energy Growth in Viscous Channel Flows," *Journal of Fluid Mechanics*, Vol. 252, July 1993, pp. 209–238.
- [9] Trefethen, L. N., Trefethen, A. E., Reddy, S. C., and Driscoll, T. A., "Hydrodynamic Stability Without Eigenvalues," *Science*, Vol. 261, No. 5121, July 1993, pp. 578–584.
- [10] Zuccher, S., Tumin, A., and Reshotko, E., "Parabolic Approach to Optimal Perturbations in Compressible Boundary Layers," *Journal of Fluid Mechanics*, Vol. 556, June 2006, pp. 189–216.
- [11] Zuccher, S., Tumin, A., and Reshotko, E., "Optimal Disturbances in Compressible Boundary Layers—Complete Energy Norm Analysis," AIAA Paper AIAA-2005-5314, 2005.
- [12] Andersson, P., Berggren, M., and Henningson, D. S., "Optimal Disturbances and Bypass Transition in Boundary Layers," *Physics of Fluids*, Vol. 11, No. 1, 1999, pp. 134–150.
- [13] Luchini, P., "Reynolds-Number-Independent Instability of the Boundary Layer Over a Flat Surface: Optimal Perturbations," *Journal of Fluid Mechanics*, Vol. 404, Feb. 2000, pp. 289–309.
- [14] Zuccher, S., Bottaro, A., and Luchini, P., "Algebraic Growth in a Blasius Boundary Layer: Nonlinear Optimal Disturbances," *European Journal of Mechanics, B/Fluids*, Vol. 25, No. 1, 2006, pp. 1–17.
- [15] Hanifi, A., Schmidt, P. J., and Henningson, D., "Transient Growth in Compressible Boundary Layer Flow," *Physics of Fluids*, Vol. 8, No. 3, 1996, pp. 51–65.
- [16] Hanifi, A., and Henningson, D., "The Compressible Inviscid Algebraic Instability for Streamwise Independent Disturbances," *Physics of Fluids*, Vol. 10, No. 8, 1998, pp. 1784–1786.
- [17] Reshotko, E., and Tumin, A., "The Blunt Body Paradox—A Case for Transient Growth," *Laminar-Turbulent Transition, IUTAM Symposium, Sedona, AZ, Sept. 1999*, edited by H. F. Fasel, and W. S. Saric, Springer-Verlag, Berlin, 2000, pp. 403–408.
- [18] Tumin, A., and Reshotko, E., "Spatial Theory of Optimal Disturbances in Boundary Layers," *Physics of Fluids*, Vol. 13, No. 7, 2001, pp. 2097–2104.
- [19] Tumin, A., and Reshotko, E., "Optimal Disturbances in the Boundary Layer Over a Sphere," AIAA Paper AIAA-2004-2241, 2004.
- [20] Tumin, A., and Reshotko, E., "Optimal Disturbances in Compressible Boundary Layers," *AIAA Journal*, Vol. 41, No. 12, 2003, pp. 2357–2363.
- [21] Reshotko, E., and Tumin, A., "The Role of Transient Growth in Roughness-Induced Transition," *AIAA Journal*, Vol. 42, No. 4, 2004, pp. 766–770.
- [22] Cathalifaud, P., and Luchini, P., "Algebraic Growth in Boundary Layers: Optimal Control by Blowing and Suction at the Wall," *European Journal of Mechanics, B/Fluids*, Vol. 19, No. 4, 2000, pp. 469–490.
- [23] Zuccher, S., Luchini, P., and Bottaro, A., "Algebraic Growth in a Blasius Boundary Layer: Optimal and Robust Control by Mean Suction in the Nonlinear Regime," *Journal of Fluid Mechanics*, Vol. 513, Aug. 2004, pp. 135–160.
- [24] Mack, L. M., "Boundary Layer Stability Theory," Jet Propulsion Lab., California Institute of Technology, JPL Rept. 900-277, Pasadena, CA, 1969.
- [25] Ting, L., "On the Initial Conditions for Boundary Layer Equations," *Journal of Mathematics and Physics*, Vol. 44, Dec. 1965, pp. 353–367.
- [26] Luchini, P., and Bottaro, A., "Görtler Vortices: A Backward-In-Time Approach to the Receptivity Problem," *Journal of Fluid Mechanics*, Vol. 363, May 1998, pp. 1–23.
- [27] Landahl, M. T., "A Note on an Algebraic Instability of Inviscid Parallel Shear Flow," *Journal of Fluid Mechanics*, Vol. 98, May 1980, pp. 243–251.
- [28] Luchini, P., and Bottaro, A., "Linear Stability and Receptivity Analyses of the Stokes Layer Produced by an Impulsively Started Plate," *Physics of Fluids*, Vol. 13, No. 6, 2001, pp. 1668–1678.
- [29] Hayes, W. D., and Probstein, R. F., *Hypersonic Flow Theory*, Academic Press, New York, 1959.

X. Zhong
Associate Editor